Chapter 16

Spectral Responses in Quantum Efficiency of Emerging Kesterite Thin-Film Solar Cells

Sanghyun Lee and Kent J. Price

Additional information is available at the end of the chapter

http://dx.doi.org/10.5772/68058

Abstract

The spectral responses in quantum efficiency provide essential information about current generation, recombination, and diffusion mechanisms in a photodetector, photodiode, and photovoltaic devices as the quantum efficiency is a function of the voltage and light biases and the spectral content of the bias light and/or location of the devices. Recently, P-type Kesterite thin-film solar cells are emerging as they have a high absorption coefficient ($>10^4$ cm^{-1}) and ideal direct bandgap (1.4–1.5 eV), which make them a perfect candidate for photovoltaic application. However, a champion device from Zincblende (CdTe) or Chalcopyrite (CIGS) solar cells shows ~21% efficiency (<21.5%, First Solar and <21.7%, ZSW, respectively) while Kesterite devices suffer from severe losses with <12.6% efficiency. Furthermore, the maximum theoretical efficiency based on Shockley-Queisser limit is about 32.2%, which indicates there is much room for the improvement. Consequently, the implication from the current situation highlights the need for a systematic analysis of the loss mechanism in Kesterite devices. In this work, we carried out a systematic study of the efficiency limiting factors based on quantum efficiency to model the quantum efficiency response of current CZTSSe thin-film solar cells. This will provide the guidance for proper interpretation of device behaviors when it is measured by quantum efficiency.

Keywords: solar cells, thin film, spectral response, quantum efficiency, photovoltaics

1. Introduction

Recently, polycrystalline thin-film CdTe and $Cu(In,Ga)Se_2$ (CIGS) solar cells are commercially successful with dramatic conversion efficiency improvements and cost reduction in module mass production as well as the balance of system (BoS), which is the cost except the module production cost. A champion device from CdTe (Zincblende) and CIGS (Chalcopyrite) solar cells shows >21%

efficiency (<21.5%, First Solar and < 21.7%, ZSW, respectively). However, some of these materials used in thin-film solar cells technology are not benign to the environment, which cause toxicity issues and possible scarce in the earth's crust, whereas competing Si solar cell technology uses the second most abundant element, Silicon, in the earth's crust. To fully facilitate the advantage of low manufacturing cost in the polycrystalline thin-film solar cells technology, a research on Kesterite solar cells using earth's abundant materials has gained momentum to pursue low-cost, environment-friendly, and highly efficient Kesterite photovoltaic devices [1–4]. P-type Kesterite solar cells have high absorption coefficient, 10^4 cm^{-1} and ideal direct bandgap (1.0–1.5 eV), which make them a perfect candidate for photovoltaic application [1–6]. Kesterite solar cells are also called CZTSSe (Copper Zinc Tin Sulphur Selenium) solar cells following the crystal structure. However, the record power conversion efficiency is 12.6% with laboratory-level samples [1, 6], which are processed with non-vacuum-based techniques. Since the development is in an early stage, the development of Kesterite solar modules is not considered yet due to incompetence in the market. However, the maximum theoretical efficiency based on Shockley-Queisser limit is about 32.2%, which indicates there is much room for improvement and hence many opportunities [7, 8].

To reduce the discrepancy between actual and maximum possible efficiency, there are major issues that need to be addressed such as absorber quality (electronic band structure, secondary phases, defect concentration, grain boundaries, optical property), CdS or (CdS-less) buffer quality, Molybdenum (Mo) back contact quality, and the quality of interfaces. One of the main challenges is different types of recombination processes at different interfaces such as buffer/window, heterojunction, and absorber/back contact. At these interfaces, recombination active defects are present due to intrinsic lower symmetry effects [9], lattice mismatch, band tails (still open discussion) [10–13], and segregation of impurities aggravated by grain boundaries, which are inevitable for polycrystalline solar cells. The recombination current enhances forward diode current that deteriorates the conversion efficiency, which is inevitable for polycrystalline Kesterite solar cells. The recombination current enhances forward diode current which worsens the conversion efficiency, which is one of the reasons to have lower open circuit voltage (*Voc*). Open circuit voltage results from the forward bias owing to the bias of the solar cell junction with the light-generated current. This is a point where diode current is equivalent to light-generated current (J_L), affected by the saturation current (J_0) of the solar cell. Since *Voc* is expressed through the saturation current as $Voc = (kT/q) \ln[(J_L/J_0) + 1]$, *Voc* depends on the recombination in the device, which is strongly dependent on the saturation current. Another factor that influences the diode saturation current is a function of the bandgap, which increases with bandgap.

Despite a recent significant improvement in Kesterite solar cells, one of the most fundamental problems that remain is lower *Voc* [14–17]. Moving *Voc* beyond 750 mV in Kesterite solar cells requires improvements in both built-in voltage and recombination. At the heterojunction of thin-film solar cells, the recombination that contributes to the diode current can occur on different recombination paths. Recombination may occur at the heterojunction interface, in the space charge region (SCR), in the quasi-neutral region (QNR), and at the back contact. In particular, the interface and near-interface recombination (SCR) mainly contribute to the recombination current, which is influenced by a number of recombination active defects and grain boundaries, the number of minority carriers at the junction edge, and diffusion length. One way to characterize the dominant recombination path is the quantum efficiency analysis.

In this chapter, we present the study of photocurrent loss mechanism based on analytical and numerical models of quantum efficiency, which provide insights into the generation and transport of carriers in the CZTSSe solar cell. Numerical models are computational results of solving continuity equation and Poisson equation, whereas analytical models are based on key parameters such as the lifetime of carriers, depletion width, diffusion length and drift length, surface recombination velocity, and thickness of the absorber layer. Key parameters of CZTSSe solar cells are focused to quantitatively describe the spectral responses of quantum efficiency by considering the recombination losses near or at the CdS/CZTSSe interface as well as the CZTSSe absorber layer. The dependency of charge collection efficiencies in the space charge region and CZTSSe absorber is discussed with respect to uncompensated impurity concentration, defect energy state, drift and diffusion components of short circuit current, and recombination velocities.

2. Analytical description of spectral responses in quantum efficiency

For this analytical study, we developed the collection efficiency model for thin-film solar cells and put in the mathematical expression. The external quantum efficiency, $EQE(\lambda, V)$ is the ratio of the number of charge carriers collected by the photovoltaic device to the number of photons of a given wavelength or energy onto the device. When the various wavelengths of light in the spectrum are applied, quantum efficiency corresponds to the spectral responses (amperes per watt) of solar cells per unit area, unit second, unit wavelength (Remember the units in solar spectra radiation).

$$EQE(\lambda, V) = \frac{I_{ph}}{q\Phi_p} = \frac{I_{ph}}{q}\left(\frac{h\upsilon}{P_{opt}}\right) \tag{1}$$

where I_{ph} is the photocurrent, Φ_p is the photon flux which is equivalent to $P_{opt}/h\nu$, and P_{opt} is the optical power.

The external quantum efficiency is related to transmission, $T(\lambda)$ of all the materials prior to CZTSSe absorber film, which consists of anti-reflection coating (ARC), transparent conducting front contact oxide (TCO), a buffer layer, and an n-type CdS layer. The internal quantum efficiency, $IQE(\lambda, V)$ is associated with the external quantum efficiency as follows.

$$EQE(\lambda, V) = \left(1 - R_{AFC}(\lambda)\right) \cdot T_{TCO}(\lambda) \cdot T_{buffer}(\lambda) \cdot T_{CdS}(\lambda) \cdot IQE(\lambda, V) \tag{2}$$

where T_{TCO} is the transmission of transparent conduction oxide (TCO), T_{buffer} is the transmission of buffer (ZnO), and T_{CdS} is the transmission of CdS.

2.1. Experimental details

In **Figure 1**, the quantum efficiency spectra of the CZTSSe solar cell are measured from 300 to 1400 nm. The cell design is based on the common substrate structure, which consists of soda-lime glass (SLG)/Molybdenum (Mo) layer followed by depositing CZTSSe film (1.8–2.0 um).

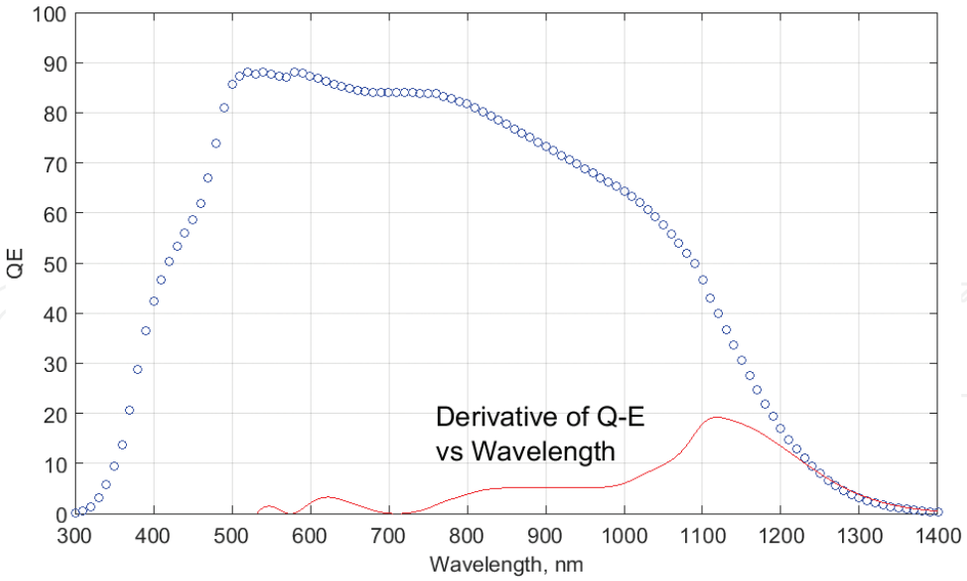

Figure 1. Spectral responses of the external quantum efficiency of a CdS/CZTSSe device measured from 300 to 1400 nm.

The buffer CdS was developed by 0.05 μm and intrinsic ZnO (0.05–0.1 μm) is deposited to prevent damage during ITO deposition at the post-ZnO deposition. Indium tin oxide (ITO) is deposited (350–400 nm) as a transparent conductive window layer; the device is completed with Ni/Al front metal fingers and MgF_2 ARC.

The spectral responses of this sample were characterized in the range of 300–1400 nm with Xenon arc lamp and the spectral distribution of the photon flux at the outlet slit was calibrated with NIST calibrated photodiode G425.

In the wavelength region 300–500 nm, measured spectral responses from the devices demonstrate typical CdS layer response, which agrees with the literature [1–5]. Above 500 nm, the measured spectral response is limited by the band gap of CZTSSe, λ_{Eg} (= hv/Eg). The bandgap calculated from the derivative of Q-E is 1.11 eV for this device and the total quantum efficiency-calculated short circuit current is 33.59 mA/cm^2. Across wavelength regions, the overall reduction in the quantum efficiency in **Figure 1** is due to the grid shading and front surface reflection as described in the literature [18]. Between 300 and 500 nm, the widely accepted loss mechanisms in quantum efficiency are TCO/ZnO absorption and CdS buffer absorption. Higher the transmission of light through TCO, ZnO, and CdS, lower the quantum efficiency losses. Hence the transmission in Eq. (2) needs to be minimized to maximize the spectral response from the device.

2.2. Energy band diagram

Under the steady-state illuminated condition, we derive the total current density under the applied biased conditions. One of the important parameter sets that determines the spectral responses in photovoltaic devices is the space charge region width, *W*. Although it is widely accepted that CdS does not fundamentally contribute photogenerated current, any changes in effective donor impurity concentration or uncompensated impurity (N_d-N_a) and photoconductivity of CdS buffer layer

greatly impact the space charger region due to an asymmetrical p-n heterojunction nature. In fact, there are a number of defects in CdS, which contribute to the increase of effective uncompensated donor concentration. In this case, the depletion layer of n-CdS/p-CZTSSe is located in almost all the p-CZTSSe absorber layer, which is fundamentally similar to an abrupt n+/p junction diode or a Schottky diode. Following the band structure [19], the depletion width (**Figure 2**) in the n-CdS/p-CZTSSe is derived as follows [20].

$$W = \sqrt{\frac{2\epsilon\epsilon_r(\phi_0 - qV)}{q^2(N_a - N_d)}} \tag{3}$$

where ϵ_r is the relative permittivity, ϵ is the permittivity of free space, $\phi_0 = qV_{bi}$ is the barrier height at the absorber side (V_{bi} is the built-in potential), V is the applied voltage, and $N_a - N_d$ is the uncompensated acceptor concentration in the CZTSSe absorber layer.

2.3. Analytical description of bias-dependent quantum efficiency

Under the steady-state illuminated condition, we derive the total current density under widely accepted assumptions, which are no thermal generation current and no photocurrent contribution by n-type CdS layer. Hence, the electron-hole generation rate by absorption is described by the below.

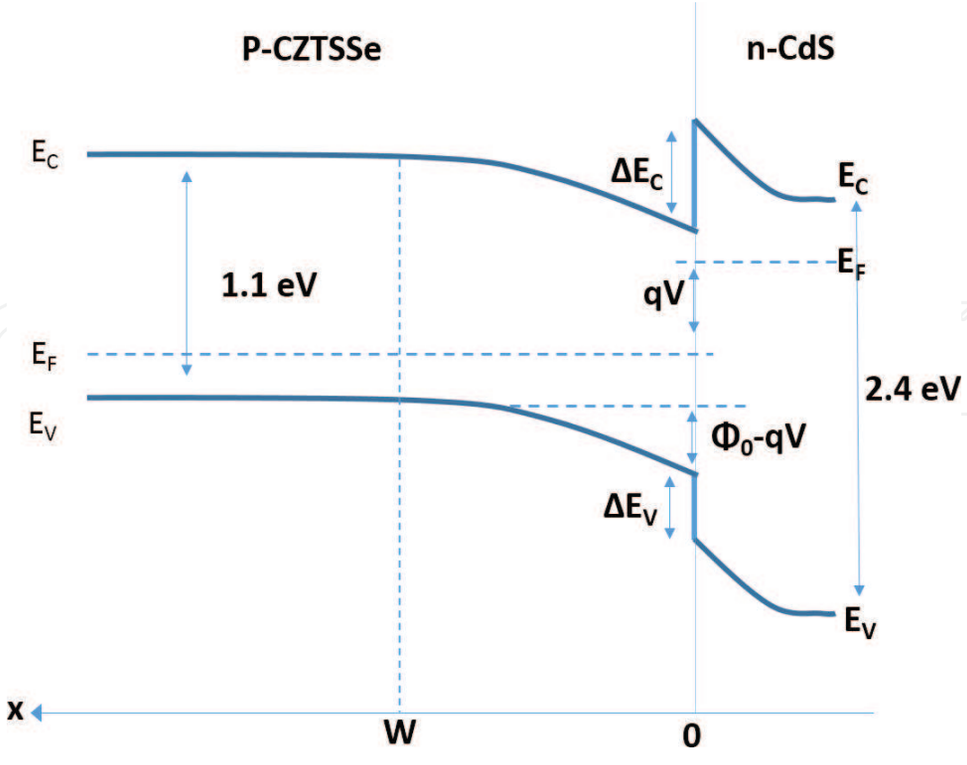

Figure 2. Energy band diagram of n-CdS/p-CZTSSe heterojunction at biased condition (V).

$$G_e(x) = \Phi_p \alpha \exp(-\alpha x) \tag{4}$$

where Φ_p is the incident photon flux per unit area and α is the absorption coefficient of CZTSSe.

To isolate non-transmission terms in the quantum efficiency Eq. (2), we distinguish $EQE(\lambda, V)$ and $IQE(\lambda, V)$ so that we will be able to focus on developing a model for carrier collection function with $IQE(\lambda, V)$. As mathematically derived by Gartner [21] and Sze [20] with boundary conditions, quantum efficiency is the sum of a drift component in the space charge region and a diffusion component in the quasi-neutral region. After simplifying the exact solution of Lavagna's model [22], Kosyachenko derived IQE [23].

$$IQE = \frac{1 + \frac{S}{D_n}\left(\alpha + \frac{2}{W} \cdot \frac{qV_{bi} - qV}{kT}\right)^{-1}}{\frac{S}{D_n}\left(\frac{2}{W} \cdot \frac{qV_{bi} - qV}{kT}\right)^{-1}} - \frac{\exp(-\alpha W)}{1 + \alpha L_n} \tag{5}$$

With the assumption of an abrupt p-n junction, the internal quantum efficiency is described based on the widely accepted Gartner formula [21, 22] as no significant contribution of electron collection by CdS is expected [23, 24].

$$IQE = 1 - \frac{\exp(-\alpha W)}{1 + \alpha L_n} \tag{6}$$

where W is the space charge region width and L_n is the diffusion length of the electron ($\sqrt{D_n \tau_n}$). Photogenerated carriers in the space charge region are assumed to be completely collected as a drift component after integrating the drift current (J_{drift}) [20].

$$J_{drift} = -q\int_0^W \phi_0 \alpha \exp(-\alpha x) dx = q\phi_0\{1 - \exp(-\alpha W)\} \tag{7}$$

$$IQE_{drift} = 1 - \exp(-\alpha W) \tag{8}$$

Photogenerated carriers outside of space charge region are collected by the diffusion process with no electric field [22] as follows.

$$IQE_{diff} = IQE - IQE_{drift} = 1 - \frac{\exp(-\alpha W)}{1 + \alpha L_n} - \{1 - \exp(-\alpha W)\} = \frac{\exp(-\alpha W)}{1 + 1/\alpha L_n} \tag{9}$$

Consequently, the total internal quantum efficiency is the sum of Eqs. (8) and (9). With complete collection of the carrier in the space charge region, EQE is revised after introducing the interface recombination term.

$$EQE(\lambda, V) = \left(1 - R_{ARC}(\lambda)\right) \cdot T_{TCO}(\lambda) \cdot T_{buffer}(\lambda) \cdot T_{CdS}(\lambda) \cdot IQE(\lambda, V) \cdot h(v) \tag{10}$$

$$h(v) = \left(1 + \frac{S_{junction}}{\mu_e E_{junction}}\right)^{-1} \tag{11}$$

where $h(V)$ is the interface recombination function due to the lattice mismatch between CdS and CZTSSe absorber, $IQE_{absorber}$ is the internal quantum efficiency of CZTSSe absorber [25], and $S_{junction}$ is the surface recombination velocity, μ_e is electron mobility, and $E_{junction}$ is the electric field at the junction.

However, a complete collection model in the space charge neglects including the space charge region recombination, and a couple of researchers identified that significant uncompensated acceptors and defects cause the recombination in the space charge region [23]. Hardrich revised a collection function (CF_{SCR}) [24] for space charge region with the hypothesis of constant field.

$$CF_{SCR\_CEF} = \exp\left(-\frac{t}{\tau_e}\right) = \exp\left(-\frac{2x}{\mu_e \tau_e E_{max}}\right) = \exp\left(-\frac{x}{L_{drift}}\right) \tag{12}$$

where τ_e is the lifetime of the electron minority carrier in the p-doped CZTSSe absorber, t is the time, constant electric field (CEF) is assumed as half of maximum ($E_{max}/2$), and L_{drift} is defined as $\mu_e \tau_e E_{max}/2 = \mu_e \tau_e (V_{bi} - V)/W$. Hence, $IQE_{absorber}$ in the space charge region under constant field yields,

$$IQE_{drift\_CEF} = \int_0^W \alpha exp(-\alpha x) \cdot \exp\left(-\frac{x}{L_{drift}}\right) dx \tag{13}$$

$$IQE_{drift\_CEF} = \frac{L_{drift}}{L_{drift} + (1/\alpha)} \cdot \left\{1 - \exp\left(-W.\left(\alpha + \frac{1}{L_{dirft}}\right)\right)\right\} \tag{14}$$

However, the electric field in the space charge region is not constant. Assuming constant doping at the junction, it linearly decreases along the depth of the CZTSSe absorber. Constant doping does not reflect the exact real situation of the doping profile due to doping concentration fluctuation with grain boundaries, fixed charges, impurities, and so on. We mathematically simplify the case with the linear electric field (LEF) at the junction. Hence, we are able to develop an alternative expression for the linearly decreasing electric field in the space charge region. An alternative expression for the collection in the space charge region begins with the definition of the drift velocity, assuming the one-dimensional charge movement, which limits the lateral movement caused by non-uniformity. To simplify the mathematical processes, we define new x-coordinate, $x' = 0$ at the interface between the space charge region and the quasi-neutral region (x' = W-x). Therefore, the drift time for the electron is as below.

$$t_{drift} = \int_0^{t_{drift}} dt = \int_x^W \frac{1}{v_{x'}} dx' = \int_{x'}^W \frac{1}{\mu_e E(x')} dx' \tag{15}$$

where an electron generated at point x′ is swept to the edge of the space charge region. The electric field inside the space charge region decreases linearly toward the quasi-neutral region of the p-type absorber layer and $E(x')$ can be revised to be $Emax \cdot (x'/W)$.

$$t_{drift} = \int_{x'}^{W} \frac{dx'}{(E_{max}\mu_e/W)\cdot x'}\, dx' = \frac{1}{E_{max}\mu_e/W} ln\left(\frac{W}{x'}\right) \tag{16}$$

$$CF_{SCR\_LEF} = exp\left(-\frac{t_{drift}}{\tau_e}\right) = exp\left(-\frac{W}{\mu_e\tau_e E_{max}} ln\left(\frac{W}{x'}\right)\right) = \left(\frac{x'}{W}\right)^{\frac{W}{\mu_e\tau_e E_{max}}} \tag{17}$$

By defining κ (= $\mu_e\tau_e E_{max}$), the collection function under the linear electric field is

$$CF_{SCR\_LEF} = \left(\frac{x'}{W}\right)^{\frac{W}{\kappa}} \tag{18}$$

And if you integrate throughout x (replacing x' into W-x) and use gamma function (Γ),

$$IQE_{drift\_LEF} = -\int_{W}^{0} \alpha e^{-\alpha(W-x')} \cdot \left(\frac{W-x'}{W}\right)^{\frac{W}{\kappa}} dx' = -\frac{\Gamma(1+\frac{W}{\kappa},\ -\alpha(x-W))}{\alpha^{\frac{W}{\kappa}} W^{\frac{W}{\kappa}}}\Bigg|_{0}^{W} \tag{19}$$

$$IQE_{drift\_LEF} = (\alpha W)^{-\frac{W}{\kappa}} \cdot \Gamma(1+\frac{W}{\kappa},\ \alpha W) \tag{20}$$

For a diffusion component of the photoelectric quantum response, the exact solutions for electron and hole are described [20] for the case of p-layer in a p-n junction, including surface recombination at the back surface CZTSSe absorber. We assume only electron contribution of the absorber layer, considering the hole collection is negligible due to strong compensation with a large number of high p-type compensating defects in CdS [23].

$$IQE_{diff} = \frac{\alpha L_n}{\alpha^2 L_n^2 - 1}\exp(-\alpha W)\cdot$$

$$\left\{\alpha L_n - \frac{\frac{S_b L_n}{D_n}\left[\cosh\left(\frac{d-W}{L_n}\right) - \exp(-\alpha(d-W))\right] + sinh\left(\frac{d-W}{L_n}\right) + \alpha L_n \exp(\alpha(d-W))}{\frac{S_b L_n}{D_n}\sinh\left(\frac{d-W}{L_n}\right) + \cosh\left(\frac{d-W}{L_n}\right)}\right\} \tag{21}$$

where d is the thickness of the CZTSSe absorber layer and S_b is the recombination velocity at the back surface of the absorber. The sum of drift and diffusion components is the total internal quantum efficiency. The total internal quantum efficiency of the absorber for the constant electric field is the sum of Eqs. (14) and (21), and the IQE for the linear electric field is the sum of Eqs. (20) and (21).

$$IQE_{CEF} = \frac{L_{drift}}{L_{drift} + (1/\alpha)} \cdot \left\{1 - \exp\left(-W \cdot \left(\alpha + \frac{1}{L_{dirft}}\right)\right)\right\} + \frac{\alpha L_n}{\alpha^2 L_n^2 - 1}\exp(-\alpha W)$$

$$\cdot\left\{\alpha L_n - \frac{\frac{S_b L_n}{D_n}\left[\cosh\left(\frac{d-W}{L_n}\right) - \exp(-\alpha(d-W))\right] + sinh\left(\frac{d-W}{L_n}\right) + \alpha L_n \exp(\alpha(d-W))}{\frac{S_b L_n}{D_n}\sinh\left(\frac{d-W}{L_n}\right) + \cosh\left(\frac{d-W}{L_n}\right)}\right\} \tag{22}$$

$$IQE_{LEF} = (\alpha W)^{-\frac{W}{\kappa}} \cdot \Gamma(1 + \frac{W}{\kappa},\ \alpha W) + \frac{\alpha L_n}{\alpha^2 L_n^2 - 1} \exp(-\alpha W) \cdot$$

$$\left\{ \alpha L_n - \frac{\frac{S_b L_n}{D_n}\left[\cosh\left(\frac{d-W}{L_n}\right) - \exp(-\alpha(d-W))\right] + sinh\left(\frac{d-W}{L_n}\right) + \alpha L_n \exp(\alpha(d-W))}{\frac{S_b L_n}{D_n}\sinh\left(\frac{d-W}{L_n}\right) + \cosh\left(\frac{d-W}{L_n}\right)} \right\} \tag{23}$$

Consequently, external quantum efficiency is the product of the total internal quantum efficiency, which includes recombination in the space charge region (Eqs. (22) and (23)), recombination at the interface (Eq. (1)), and the optical losses prior to CZTSSe absorption.

$$EQE_{CEF} = (1 - R_{ARC}) T_{TCO} T_{Buffer} T_{CdS} \cdot$$
$$\left\{ \frac{L_{drift}}{L_{drift} + \left(\frac{1}{\alpha}\right)} \cdot \left[1 - exp\left(-W \cdot \left(\alpha + \frac{1}{L_{dirft}}\right)\right)\right] + \frac{\alpha L_n}{\alpha^2 L_n^2 - 1} exp(-\alpha W) \cdot \right.$$
$$\left. \left\{ \alpha L_n - \frac{\frac{S_b L_n}{D_n}\left[\cosh\left(\frac{d-W}{L_n}\right) - \exp(-\alpha(d-W))\right] + sinh\left(\frac{d-W}{L_n}\right) + \alpha L_n \exp(\alpha(d-W))}{\frac{S_b L_n}{D_n}\sinh\left(\frac{d-W}{L_n}\right) + \cosh\left(\frac{d-W}{L_n}\right)} \right\} \right\}$$
$$\cdot \left(1 + \frac{S_{junction}}{\mu_e E_{junction}}\right)^{-1} \tag{24}$$

$$EQE_{LEF} = (1 - R_{ARC}) T_{TCO} T_{Buffer} T_{CdS} \cdot \left\{ (\alpha W)^{-\frac{W}{\kappa}} \cdot \Gamma(1 + \frac{W}{\kappa},\ \alpha W) + \frac{\alpha L_n}{\alpha^2 L_n^2 - 1} \exp(-\alpha W) \cdot \right.$$
$$\left. \left\{ \alpha L_n - \frac{\frac{S_b L_n}{D_n}\left[\cosh\left(\frac{d-W}{L_n}\right) - \exp(-\alpha(d-W))\right] + sinh\left(\frac{d-W}{L_n}\right) + \alpha L_n \exp(\alpha(d-W))}{\frac{S_b L_n}{D_n}\sinh\left(\frac{d-W}{L_n}\right) + \cosh\left(\frac{d-W}{L_n}\right)} \right\} \right\}$$
$$\cdot \left(1 + \frac{S_{junction}}{\mu_e E_{junction}}\right)^{-1} \tag{25}$$

For the non-uniform field, mathematical expressions are developed with an exponential electric field [26] or two different electric field regions [27, 28]. However, it is argued that including the non-uniform electric field with additional parameter sets only adds confusion with no additional insights [29]. Hence, we will explore the quantum efficiency response with a constant electric field model for our analysis for simplification.

2.4. Impurity concentration and electron lifetime by analytical models

Figure 3 shows the computed spectral responses of the external quantum efficiency, $EQE(\lambda)$ with the impact of the uncompensated acceptor impurity at the n-CdS/p-CZTSSe interface. The absorption coefficient, $\alpha(\lambda)$ was taken from Ref. [28] and the front surface recombination velocity (S_f), the default depletion width is 0.3 μm, and the electron lifetime (τ_n) were 10^3 cm/s and 10^{-9} s [29, 30]. In **Figure 3**, the Q-E shape changes disproportionally with significant red light response reduction >600 nm as the uncompensated impurity concentration changes

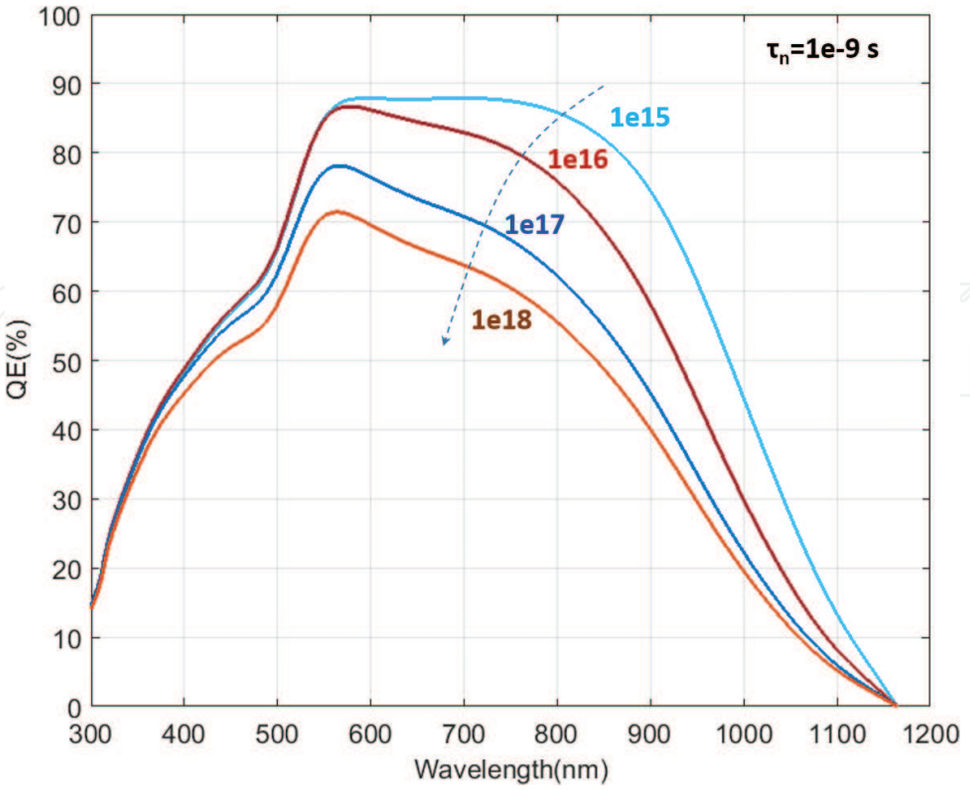

Figure 3. EQE for uncompensated acceptor concentration (N_a–N_d), 10^{15}, 10^{16}, 10^{17}, and 10^{18} cm^{-3}.

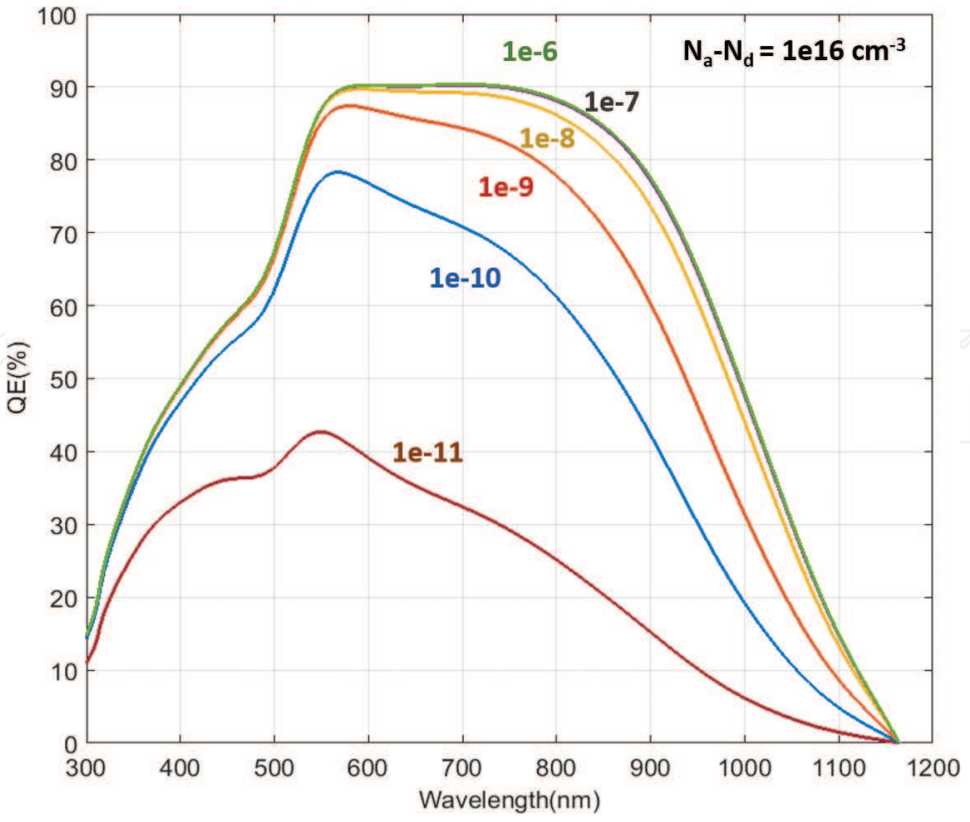

Figure 4. EQE spectra with minority carrier lifetime (τ_n), 10^{-6}, 10^{-7}, 10^{-8}, 10^{-9}, 10^{-10}, and 10^{-11} s.

(N_a–N_d). When the concentration of (N_a–N_d) increases from 10^{15} cm^{-3} to 10^{18} cm^{-3}, the external quantum efficiency decreases. The decrease in EQE(λ) is due to the expansion of the depletion layer, which induces efficient photogenerated minority carrier from the absorber bulk. However, the decrease in photosensitivity between 300 and 500 nm is relatively small, which is mainly influenced by the absorption and recombination of ZnO and CdS. This is also well demonstrated in the Q-E responses with a set of electron lifetime (τ_n) in **Figure 4**, which shows less changes in Q-E between 300 and 500 nm except the extreme case of 10 ps. With the same depletion width by the same uncompensated impurity concentration, electron lifetime that can facilitate an electron to travel throughout the quasi-neutral region to the space charge region can show higher carrier collection and fewer carrier losses in the range from 600 to 900 nm as electron lifetime decreases from 10^{-6} to 10^{-10} s.

2.5. Impact of deletion width by analytical model

In order to provide the losses caused by recombination at the CdS/CZTSSe interface, we now check the spectral response broken into drift and diffusion components in Q-E spectra. **Figure 5** demonstrates the drift component in dashed line and the diffusion component in dash-dotted line as the depletion width increases from 0.1 to 0.9 μm. At the depletion width, 0.9 μm, the photogenerated carrier in the absorber near 600–1000 nm can be efficiently collected mainly via the space charge region by showing the sufficient drift component compared to the weak diffusion component of photogenerated current. However, once the depletion width decreases

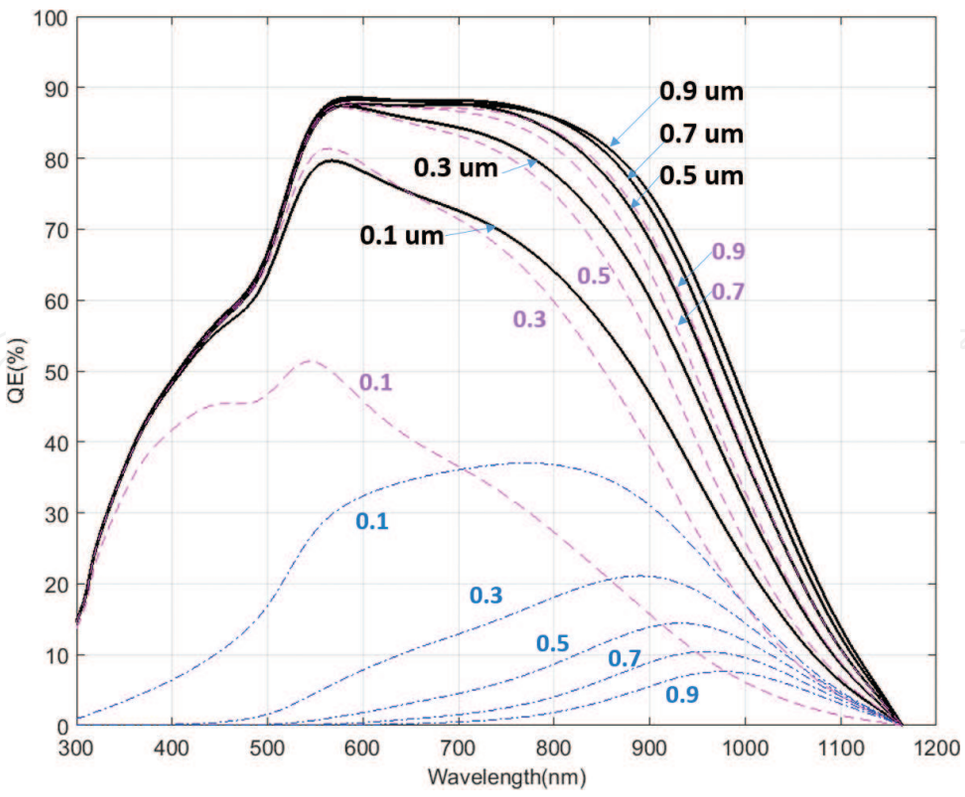

Figure 5. EQE spectra with the depletion width, 0.1, 0.3, 0.5, 0.7, and 0.9 μm broken into the diffusion and drift components. The total EQE (black) is a sum of the diffusion component (blue) and the drift component (magenta).

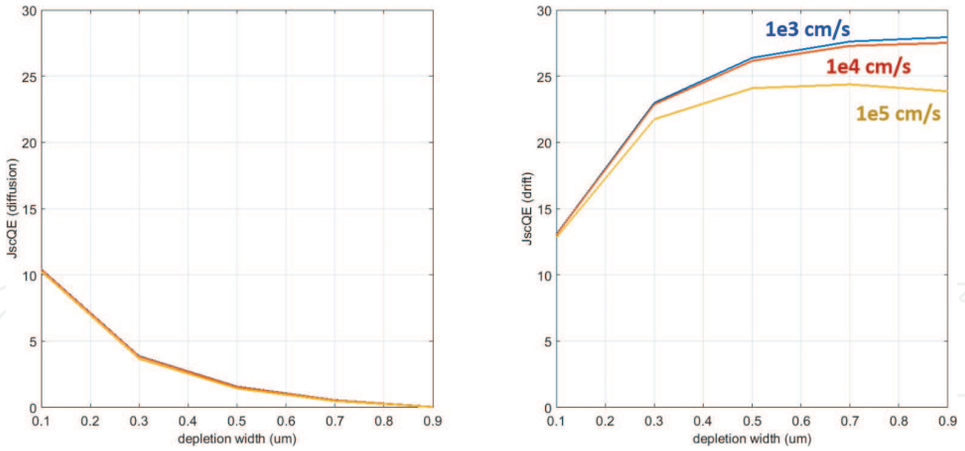

Figure 6. JscQE (drift) and JscQE (diffusion) under the standard AM 1.5 solar radiation (1 sun, 100 mW/cm^2) under different front surface recombination velocities (10^3, 10^4, and 10^5 cm/s).

from 0.9 μm, the drift component begins to weaken in the CZTSSe absorber in 600–1000 nm and the diffusion component increases. At the depletion width, 0.1 μm, the contribution to the carrier collection by drift component is almost equivalent to that of the diffusion component. Based on the calculation of Q-E spectra about each drift and diffusion component, **Figure 6** shows the drift current short circuit current component, JscQE (drift) and the diffusion short circuit current component, JscQE (diffusion) under the standard AM 1.5 solar radiation (1 sun, 100 mW/cm^2) under different front surface recombination velocities (10^3, 10^4, 10^5 cm/s). As *Sf* increases, there are no noticeable changes in the diffusion component whereas the drift component decreases faster.

3. Comparison with modeling and simulation of CZTSSe devices

In this section, we investigate quantum efficiency by utilizing SCAPS simulator (Solar Cell Capacitance Simulator) version 3.2.01 to computationally model the quantum efficiency response of current CZTSSe thin-film solar cells. This will also provide the proper interpretation of device behaviors when it is measured by quantum efficiency. In particular, we focus on the influence of near-interface defect states on quantum efficiency at particular bias conditions with the intention of evaluating peculiar quantum efficiency responses by defect distributions with adjusting 1D numerical parameters in this work.

Each material parameter as an input includes thickness, relative permittivity, electron mobility, hole mobility, acceptor concentration, donor concentration, band gap, and effective density of states. The simulated device structure of CZTSSe thin-film solar cell is with ZnO window layer, CdS buffer, CZTSSe absorber, and Molybdenum (Mo) back contact. In intrinsic defects in the CZTSSe bulk, we updated the parameter sets from the analytical description to reflect the real situation to understand the general trend by interface defect states. Parameters used for this device structures are listed in **Table 1**. Considering the complexity of interface defects at absorber/back contact, absorber/buffer, and buffer/window, we adopted the basic input parameters from the literature, theories, or reasonable estimates [12, 28, 31]. In reality, there is a significant amount of intrinsic bulk defects with different charge states in the CZTSSe

Parameters	Symbol (unit)	ZnO	CdS	CZTSSe
Thickness	d (nm)	200	50	2500
Band gap	Eg (eV)	3.3	2.4	1.2–1.3
Electron affinity	χ (eV)	4.4	4.2	4.1
Relative permittivity	ϵ/ϵ_r	9	10	10
Effective density of state (CB)	N_C (10^{18} cm^{-3})	2.2	2.2	2.2
Effective density of state (VB)	N_V (10^{19} cm^{-3})	1.8	1.8	1.8
Electron thermal velocity	v_n (10^7 cm/s)	1.0	1.0	1.0
Hole thermal velocity	v_p (10^7 cm/s)	1.0	1.0	1.0
Electron mobility	μ_n (cm^2/V-s)	100	100	100
Hole mobility	μ_p (cm^2/V-s)	25	25	25
Donor concentration	N_D (10^{17} cm^{-3})	10.0	1.0	0
Acceptor concentration	N_A (10^{14} cm^{-3})	0	0	2.0
Bulk defect type	a, d, n	d	a	d/a/n
Bulk defect concentration	N_t (10^{14} cm^{-3})	10,000	100	1/1/5

Types of defect are: a, acceptor; d, donor; n, neutral.

Table 1. Parameters set used in this work.

absorber layer as well as ZnO, CdS layers. To introduce different amounts of intrinsic defects in the CZTSSe bulk, we updated the parameter sets from the analytical description to reflect the real situation to understand the general trend by interface defect states. Parameters used for this device structure are listed in **Table 1**. Considering the complexity of interface defects at absorber/back contact, absorber/buffer, and buffer/window, we adopted the basic input parameters from the literature, theories, or reasonable estimates [31–36].

3.1. Interface trap-free case

In the first step, the numerical simulations of both current-voltage (I-V) and quantum efficiency (Q-E) characteristics have been carried out without traps near the heterojunction interface. The default illumination spectrum and operation temperature are set to the standard AM 1.5 condition and 300 K, respectively. A typical result of the I-V curve simulated for a CZTSSe solar cell without heterojunction defects is demonstrated in **Figure 7(a)**. As expected, we observed an ideal steep I-V curve with conversion efficiency, 15.3% with emphasis on higher *Voc* (661 mV) and FF (72.5%) than any reported experimental *Voc* and FF justifying the assumption of an intrinsic defect-free interface.

The simulated I-V curve in **Figure 7** shows the dramatic improvement of *Voc* with nearly zero conductance (<2.6 mS/cm^2) at short circuit condition (in other words, a slope of I-V curve at zero bias) which can be explained by the alleviated recombination and the improved carrier collection with the associated depletion width change. In particular, the reduced recombination can lower the total forward diode current by showing the ideal slope at the short circuit current

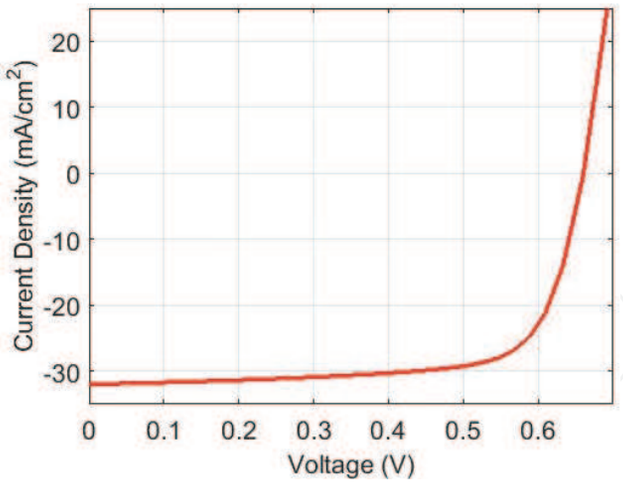

Figure 7. I-V of ideal CZTSSe solar cells without interface defects with efficiency (15.3%), Voc (661 mV), FF (72.5%), and Jsc (32.0 mA/cm^2).

condition [25]. With an ideal device having no near-interface defects in the simulation, an ideal uniform absorber setting keeps the shape and the ratio of the quantum efficiency curves, (H(V)/H(−1 V)) under biases since the shape of the curves in quantum efficiency depends on wavelength and is almost independent of bias voltage [20]. One way to confirm the uniformity of reduced carrier collection at each wavelength region is to compare carrier collection at each bias with full collection by applying negative bias, for example, −1 V [20]. In **Figures 8** and **9**, each quantum efficiency at different biases is normalized by dividing with the quantum efficiency at −1 V. The normalized Q-E (QE(V)/QE(−1 V)) shows two features by comparing each bias-dependent quantum efficiency. First, wavelength-dependent quantum efficiency drop is observed regardless of bias level. Secondly, the shape of each normalized quantum efficiency curve is kept almost the same. In other words, a nearly uniform collapse of quantum efficiency over a wide range of wavelength is demonstrated with the trend of increasing absorber collection loss due to reduced depletion width by applied biases at region 2 (500–800 nm) and region 3 (800–1033 nm).

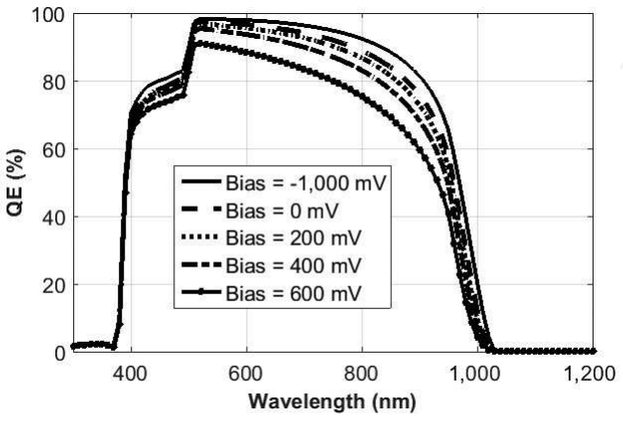

Figure 8. Q-E of ideal CZTSSe solar cells without interface defects at bias conditions (−1.0, 0.0, 0.2, 0.4, and 0.6 V).

http://dx.doi.org/10.5772/68058

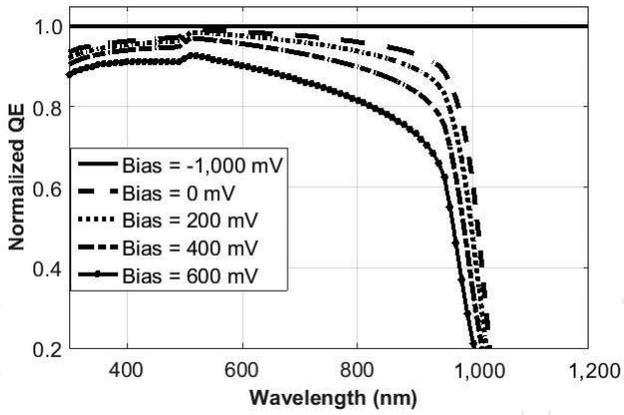

Figure 9. Normalized Q-E of ideal CZTSSe solar cells (QE(V)/QE(−1 V)) at bias conditions (−1.0, 0.0, 0.2, 0.4, and 0.6 V).

3.2. Interface and near-interface defect states case

Before discussing the simulated results, it is worth describing the systematic trends affected by varying the interface defect parameters for the different types of defects. First, we consider acceptor- and donor-type defects near both conduction and valence bands as well as mid-gap. In SCAPS simulation, we can introduce three different parameter sets of interface defects for both acceptor and donor types that significantly affect the performance of the device (capture cross sections, defect energy level: E_t, defect density). However, real CZTSSe cells consist of complex multilayers, which form defects and/or defect compounds at the surface of CZTSSe layer, next to the CdS buffer layer. Furthermore, the direct measurement of this layer's electronic properties is difficult to be separated from other layers' electronic properties which are exacerbated by complicated window structures with CdS, ZnO, and TCO layer interdiffusion. To avoid the complexity of modeling, we focus on numerical modeling of electronic properties, in particular, quantum efficiency by introducing a thin defective interface layer between CdS and absorber.

3.2.1. Trend by defect distribution and concentration

In the first step, numerical simulations have been carried out with a set of defect concentrations within a defective interface layer. To be consistent with the reported literature, theories, or reasonable estimates, capture cross sections are fixed at 1.0×10^{-12} cm^2 for electrons and 1.0×10^{-15} cm^2 for holes at donor-type defect and at 1.0×10^{-15} cm^2 for electrons and 1.0×10^{-12} cm^2 for acceptor-type defect [12, 28–31, 33–37]. For a comparative study of the ideal device in the previous section, the device structure is updated with very thin (5 nm) defective interface layer between CdS and CZTSSe. Input parameters are set to the same as those of CdS buffer except thickness and doping densities which are set to the same values of 1.0×10^{14} cm^{-3} for donor and acceptor assuming the intermixing of n-type dopant (CdS) and p-type dopant (CZTSSe).

Figure 10 shows the simulated quantum efficiency with an inserted defective interface layer between CZTSSe and CdS buffer layers as a function of defect concentration. As we begin with defect density 1.0×10^{15} cm^{-3} in this thin layer as deep acceptor-type bulk defect which is different from donor-like interface trap (as in the conventional Si model), we located this type of defect between 0.9 and 1.5 eV above the top of the valence band around the mid-gap (1.2 eV).

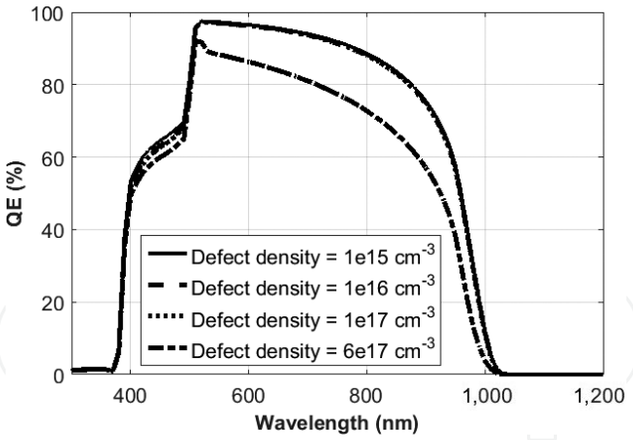

Figure 10. Q-E of CZTSSe device with the inserted interface defective layer between CdS and CZTSSe, varying acceptor-type defect density from 1.0×10^{15} to 6.0×10^{17} cm^{-3}.

As defect concentration increases until 1.0×10^{17} cm^{-3} no specific collection loss at particular regions is observed. However, once defect concentration increases more than 6.0×10^{17} cm^{-3}, serious collection loss at the absorber is demonstrated in regions 2 (500–800 nm) and 3 (800–1033 nm). In region 1 (300–500 nm), there is not much collection loss while slight inflection of collection occurs near 500 nm.

3.2.2. Impact by deep acceptor-type defect distribution

Based on the findings above, defect concentration is set at 6.0×10^{17} cm^{-3} as deep acceptor-type defects, 0.9 eV below and above from the bottom of the conduction band and top of the valence band, respectively. Consequently, the results of the simulated biased quantum efficiency are demonstrated in **Figure 11**. Beginning at −1 V (not shown), quantum efficiency over all wavelength regions shows similar spectral response compared to that of the device without defects in **Figure 8**. Once bias increases up to 0 V, absorber loss slightly increases as mentioned in **Figure 8**. As expected, this reduction in quantum efficiency is caused by the decrease of the depletion layer. However, as bias increases up to 0.2 V, the stronger drop of Q-E spectrum happens at both < 500 nm and > 550 nm disproportionately. Conversely, the reduction of quantum efficiency between 500–550 nm is less severe that the other regions. This peculiar Q-E response occurs with a peak near 520–530 nm (in other words, near blue light region), reported at their measurements in Refs. [12, 37].

Apparently, the reduction in $\lambda < 400$ nm, which is relatively non-sensitive, is due to absorption by the CdS layer and the transparent conducting oxide/substrate. In the spectral region, < 500 nm, the absorption by CdS at 0.2 V is slightly decreased due to the smaller photocurrent contribution and adjustment of space charge region of window layer under the presence of strongest electric field at the heterojunction. On the other hand, the intensified quantum efficiency drop in <500 nm and distinctively >550 nm looks interesting. When it comes to describing the bias-dependent quantum efficiency, the Gartner model describes the photogenerated carrier collection with the bias-dependent depletion width (Eq. (6)) and diffusion length, which describes the exact expression (Eq. (21)) as we discussed in the previous section [20, 36].

http://dx.doi.org/10.5772/68058

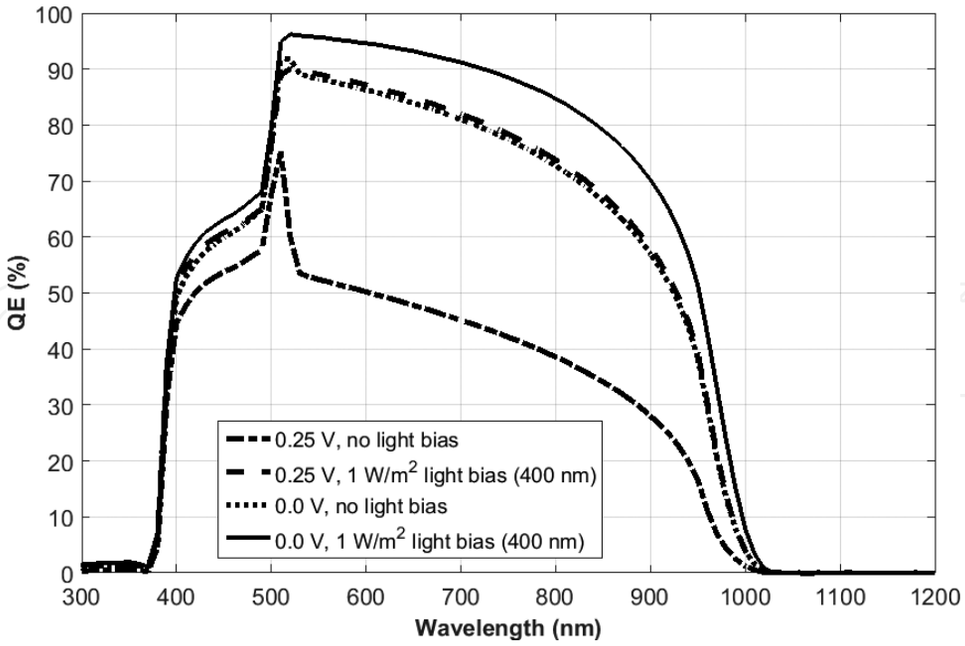

Figure 11. Light-biased (1 mW/cm^2, 0.01 sun at 400 nm) Q-E of CZTSSe solar cell with the defective interface layer at 0 and 0.25 V.

With the given depletion width (W_d), diffusion length (L_n), absorber thickness (d), and surface recombination velocity (S_n), the exact expression predicts the trend of spectral response in thin-film solar cells under the presence of voltage and, in particular, quantum efficiency response for an ideal device. However, the exact model or the Hecht-like equation in Ref. [29] is solely dependent on the depletion width (or applied bias) and diffusion length. Under applied voltage biases compared to the full collection, the analytical quantum efficiency analysis is unable to demonstrate the intensified reduction at both <500 nm and >550 nm but it rather provides partial interpretation of the quantum efficiency with the above equations by keeping a similar shape of curves. Hence, analytical expressions do not represent the peculiar Q-E response near 520–530 nm over other wavelength regions from our simulation.

However, the intensified drop in both <500 nm and distinctively >550 nm can be explained by assuming deep acceptor-type defects near the heterojunction interface layer. In this interface layer, a higher concentration of deep ionized-acceptor (negative charge) type defects 0.3 eV above and below the mid-gap impacts the electric field and hence the space charge region of absorber toward the back contact. These deep acceptor-type defects induce electronic doping at room temperature by trapping holes from the valence band, which eventually lower the band bending of the CdS/CZTSSe interface layer upon additional blue light. In other words, higher electric field near the heterojunction interface increases absorption by a part of the absorber toward CdS and near-CdS layer, whereas it reduces absorption by the majority of CZTSSe absorber toward the back contact. This reduced depletion width by higher interface defects can be deteriorated by increased biases such as 0.2 and 0.25 V, which furthers the depletion width decrease. One way to confirm depletion width reduction induced by CdS/absorber interface defects is to apply weak blue light bias (400 nm) and observe spectral

response at >550 nm in quantum efficiency. Using this model, weak light bias (1 mW/cm^2, 0.01 sun) is applied to the same device at 0 and 0.25 V in **Figure 11**. Weak blue light bias onto window and buffer layers almost fully recovers CZTSSe absorber carrier collection even at 0.25 V. After filtering out noises in the regions of <400 and >1000 nm, light-biased Q-E is normalized by dividing with the standard no-light-biased Q-E in **Figure 12**. This clearly indicates that weak blue light bias intensifies the carrier collection of absorber in regions 2 and 3 (>550 nm) at both 0 and 0.25 V, whereas minimal increases are shown in region 1 (<500 nm). At 0.25 V, the depletion width of CZTSSe absorber without light bias is narrower than that with weak blue light bias. Hence, weak light bias activates hole trapping through deep acceptor-type defects and near-interface defects between 0.9 and 1.5 eV and recovers the depletion width.

The presence of ionized deep acceptor-type bulk defects (0.9–1.5 eV) in the defective interface layer can effectively decrease the depletion width near the heterojunction interface by increasing negative charge density (**Figure 13**), which could only be activated by weak bias light via hole charge trapping. The band diagram and carrier density of holes and electrons indicate

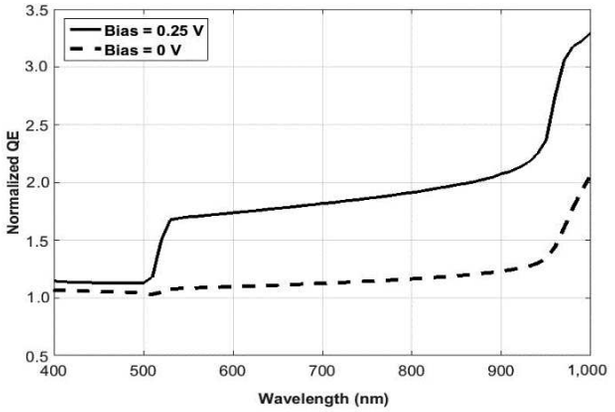

Figure 12. Light bias-dependent normalization of Q-E (Q-E at blue light bias divided by Q-E at no light bias) illustrating weak blue light bias (400 nm).

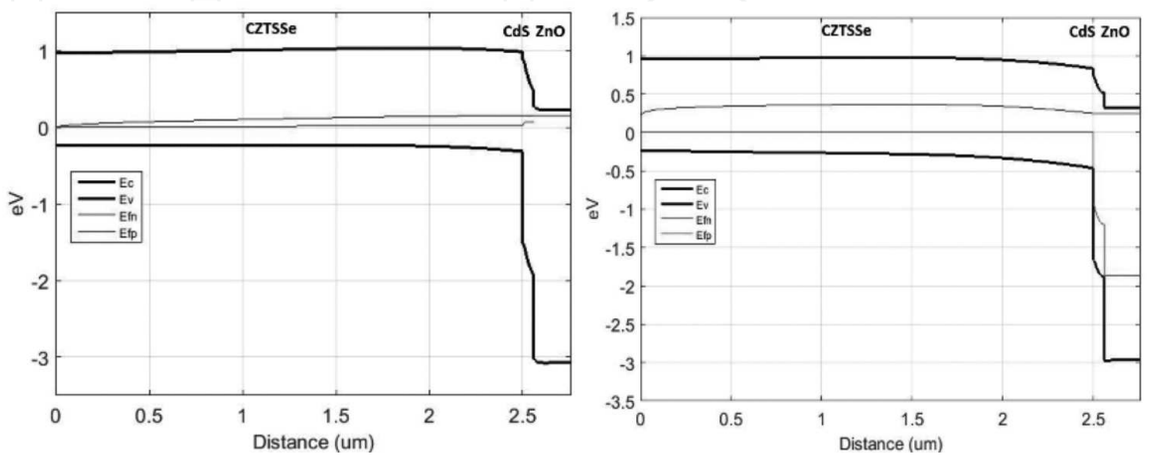

Figure 13. Band diagram without light bias at 0.25 V (left) and with light bias at 0.25 V (right), showing larger depletion width.

higher electric field with less hole concentration at the interface, resulting in smaller depletion width in the presence of the defective interface layer in **Figure 13**.

4. Summary

The spectral response of CZTSSe thin-film solar cells has been modeled analytically and numerically with simulation study under a set of different parameters and biased conditions about efficiency-limiting factors through quantum efficiency. The analytical model describes the drift and diffusion photocurrent components to reflect the recombination losses in the space charge region and near the CdS/CZTSSe heterojunction interface. The trend that we found about the uncompensated impurity concentration, minority carrier lifetime, surface recombination velocity, and the depletion width shows qualitatively good agreement with the reported data in the literature. Furthermore, the simulations address the role of interface and near-interface defects for the spectral response of thin-film solar cells. For this simulation study, it is assumed that deep acceptor-type near-heterojunction interface defects from 0.9 to 1.5 eV above the top of the valence band are difficult to increase the depletion width, which provide additional electronic doping in space charge region. These ionized acceptor-type defects at room temperature can trap holes from the valence band only activated by additional bias light and reduce the effective doping concentration at the heterojunction interface. Consequently, these deep acceptor-type defects cramp the depletion width and hence, weaker spectral responses near red and IR regions. This trend is intensified with biased quantum efficiency conditions. The findings of this work give further insight into the issues and provide some requirements on the parameter sets of the CZTSSe absorber layer as well as the CdS/CZTSSe heterojunction interface layer, which shows fairly good agreement with numerical calculation and reported experimental results.

Author details

Sanghyun Lee[1]* and Kent J. Price[2]

*Address all correspondence to: sanghyun.lee0304@gmail.com

1 School of Engineering and Information Systems, Morehead State University, Morehead, KY, USA

2 Department of Physics, Morehead State University, Morehead, KY, USA

References

[1] W. Wang, M.T. Winkler, O. Gunawan, T. Gokmen, T.K. Todorov, Y. Zhu, D.B. Mitzi. Device characteristics of CZTSSe thin-film solar cells with 12.6 % efficiency. Adv. Energy Mater. 2014;**4**:1301465.

[2] D. Mitzi, T. Todorov, K. Wang, S. Gunha. The path towards a high-performance solution-processed kesterite solar cell. Sol. Energy Mater. Sol. Cells. 2011;**95**:1421–1436.

[3] Y. Kumar, G. Babu, P. Bhaskar, V. Raja. Preparation and characterization of spray-deposited Cu_2ZnSnS_4 thin films. Sol. Energy Mater. Sol. Cells. 2009;**93**:1230–1237.

[4] C.P. Chan, H. Lam, C. Surya. Preparation of Cu_2ZnSnS_2 films by electrodeposition using ionic liquids. Sol. Energy Mater. Sol. Cells. 2010;**94**:207–211.

[5] H. Katagiri, K. Jimbo, S. Yamada, T. Kamimura, W.S. Maw, T. Fukano, T. Ito, T. Motohiro. Detailed balance limit of efficiency of p-n junction solar cells. Appl. Phys. Express. 2008;**1**:41201.

[6] M. Paranthaman, W. Wong-Ng, R. Bhattacharya, editors. Semiconductor materials for solar photovoltaic cells (1st ed.). Springer International Publishing, Switzerland; 2016. doi:10.1007/978-3-319-20331-7_2.

[7] P. Jackson, D. Hariskos, R. Wuerz, W. Wischmann, M. Powalla. Compositional investigation of potassium doped $CuInGaSe_2$ solar cells with efficiencies up to 20.8 %. Phys. Stat. Sol. RRL. 2014;**8**:219–222.

[8] W. Shockley, H.K. Queisser. Detailed balance limit of efficiency of p-n junction solar cells. Jpn. J. Appl. Phys. 1961;**32**:510–519.

[9] G. Lucovsky, S. Lee, J.P. Long, H. Seo, J. Luning. Interfacial transition regions at germanium/Hf oxide based dielectric interfaces: qualitative differences between non-crystalline Hf Si oxynitride and nanocrystalline HfO2 gate stacks. Microelectron. Eng. 2009;**86**(3):224–234.

[10] J. Moore, C. Hages, R. Agrawal, M. Lundstrom. The importance of band tail recombination on current collection and open-circuit voltage in CZTSSe solar cells. Appl. Phys. Lett. 2016;**109**:021102.

[11] T. Gokmen, O. Gunawan, T. Todorov, D. Mitzi. Band tailing and efficiency limitation in kesterite solar cells. Appl. Phys. Lett. 2013;**103**:103506.

[12] T. Gokmen, O. Gunawan, D.B. Mitzi. Semi-empirical device model for $Cu_2ZnSn(S,Se)_4$. Appl. Phys. Lett. 2014;**105**:033903.

[13] J. Moore, C. Hages, N. Carter, R. Agrawal, J. Gray, M. Lundstrom. Current–voltage analysis of band tail effects in CZTSSe through numerical simulation. 2015 IEEE 42nd Photovoltaic Specialist Conference (PVSC). 2015.

[14] D. Mitzi, O. Gunawan, T. Todorov, D. Barkhouse. Preparation of Cu_2ZnSnS_4 films by electrodeposition using ionic liquids. Phil. Trans. R. Soc. A. 2013;**371**(20110432):1–22.

[15] O. Simya, A. Mahaboobbatcha, K. Balachander. A comparative study on the performance of Kesterite based thin film solar cells using SCAPS simulation program. Superlatt. Microstruct. 2015;**82**:248–261.

[16] T. Jager, Y. Romanyuk, B. Bissig, F. Pianezzi, S. Nishiwaki, P. Reinhard, J. Steinhauser, J. Schwenk, A. Tiwari. Improved open-circuit voltage in $Cu(In,Ga)Se_2$ solar cells with high work function transparent electrodes. J. Appl. Phys. 2015;**117**:225303.

[17] F.-J. Haug, R. Biron, G. Kratzer, F. Leresche, J. Besuchet, C. Ballif, M. Dissel, S. Kretschmer, W. Soppe, P. Lippens, K. Leitner. Improvement of the open circuit voltage by modifying the transparent indium-tin oxide front electrode in amorphous n-i-p solar cells. Prog. Photo. 2012;**20**(6):727–734.

[18] S. Hegedus, W. Shafarman. Thin-film solar cells: device measurements. Prog. Photovolt. Res. Appl. 2004;**12**(2–3):155–176. doi:10.1002/pip.518.

[19] C. Hages, N. Carter, R. Agrawal, T. Unold. Generalized current–voltage analysis and efficiency limitations in non-ideal solar cells: case of $Cu_2ZnSn(S_xSe_{1-x})_4$ and $Cu_2Zn(Sn_yGe_{1-y})(S_xSe_{1-x})_4$. J. Appl. Phys. 2014;**115**:234504.

[20] S. Sze, K. Ng. Physics of semiconductor devices (3rd.). New York: John Wiley & Sons; 2007.

[21] W. Gartner. Depletion-layer photoeffects in semiconductors. Phys. Rev. 1959;**116**:84–87.

[22] M. Lavagna, J.P. Pique, Y. Marfaing. Theoretical analysis of the quantum photoelectric yield in Schottky diode. Solid State Electron. 1977;**20**:235–240.

[23] L.A. Kosyachenko. Problems of efficiency of photoelectric conversion in thin-film CdS/CdTe solar cells. Semiconductors. 2006;**40**(6):710–727.

[24] M. Hadrich, H. Metzner, U. Reislohner, C. Kraft. Modelling the quantum efficiency of cadmium telluride solar cells. Sol. Energy Mater. Sol. Cells. 2011;**95**:887–893.

[25] A.L. Fahrenbruch, R.H. Bube. Fundamentals of solar cells: photovoltaic solar energy conversion (1st ed.). Academic Press, New York; 1983.

[26] A. Nakane, H. Tampo, M. Tamakoshi, S. Fujimoto, K.M. Kim, S. Kim, H. Shibata, S. Niki, H. Fukiwara. Quantitative determination of optical and recombination losses in thin-film photovoltaic devices based on external quantum efficiency analysis. J. Appl. Phys. 2016;**120**(6):064505. doi:10.1063/1.4960698.

[27] K. Misiakos, F. Lindholm. Analytical and numerical modelling of amorphous silicon p-i-n solar cells. J. Appl. Phys. 1988;**64**:383.

[28] V. Chu, J. Conde, D. Shen, S. Wagner. Photocurrent collection in a Schottky barrier on an amorphous silicon-germanium alloy structure with 1.23 eV optical gap. Appl. Phys. Lett. 1989;**55**:262.

[29] S. Hegedus, D. Desai, C. Thompson. Voltage dependent photocurrent collection in CdTe/CdS solar cells. Prog. Photovolt. Res. Appl. 2007;**15**:587–602.

[30] A. Pu, F. Ma, C. Yan, J. Huang, K. Sun, M. Green, X. Hao. Sentaurus modelling of 6.9% Cu_2ZnSnS_4 device based on comprehensive electrical & optical characterization. Sol. Energy Mater. Sol. Cells. 2017;**160**:372–381. doi:10.1016/j.solmat.2016.10.053.

[31] O. Gunawan, T.K. Todorov, D.B. Mitzi. Loss mechanisms in hydrazine-processed $Cu_2ZnSn(Se,S)_4$ solar cells. Appl. Phys. Lett. 2010;**97**:233506.

[32] P. Viktorovich, G. Moddel, J. Blake, W. Paul. Carrier-collection efficiencies in amorphous hydrogenated silicon Schottky-barrier solar cells. J. Appl. Phys. 1981;**52**:6203.

[33] W. Zhao, W. Zhou, X. Miao. Numerical simulation of CZTS thin film solar cell. In 7th IEEE International Conference on Nano/Micro Engineered and Molecular Systems, 2012, pp. 502–505.

[34] T. Gokmen, O. Gunawan, D.B. Mitzi. Modelling polycrystalline semiconductor solar cells. Thin Solid Films. 2000;**361–362**(033903):527–532.

[35] A. Polizzott, I.L. Repins, R. Noufi, S-Hi We, D.B. Mitzi. The state and future prospects of kesterite photovoltaics. Energy Environ. Sci. 2013;**6**:3171–3182.

[36] R.D. Rugescu, L. Kosyachenko. Solar energy (1st ed.). InTech, Croatia; 2010, pp. 105–130.

[37] G. Brammertz, S. Oueslati, M. Buffiere, J. Bekaert, H.E. Anzeery, K.B. Messaoud, S. Sahayarj, T. Nuytten, C. Koble, M. Meuris, J. Poortmans. Investigation of properties limiting efficiency in $Cu_2ZnSn(S,Se)_4$-based solar cells. IEEE J. Photovolt. 2015;**527–532** (5):649–655.